Article

Improved Object-Based Estimation of Forest Aboveground Biomass by Integrating LiDAR Data from GEDI and ICESat-2 with Multi-Sensor Images in a Heterogeneous Mountainous Region

Lin Chen [1], Chunying Ren [2,*], Guangdao Bao [3], Bai Zhang [2], Zongming Wang [2,4], Mingyue Liu [5], Weidong Man [5] and Jiafu Liu [6]

1 Institute of Remote Sensing and Earth Sciences, Hangzhou Normal University, Zhejiang Provincial Key Laboratory of Urban Wetlands and Regional Change, Hangzhou 311121, China; chenlin@hznu.edu.cn
2 Key Laboratory of Wetland Ecology and Environment, Northeast Institute of Geography and Agroecology, Chinese Academy of Sciences, Changchun 130102, China; zhangbai@iga.ac.cn (B.Z.); zongmingwang@iga.ac.cn (Z.W.)
3 Jilin Provincial Academy of Forestry Sciences, Changchun 130033, China; zhaic@ccu.edu.cn
4 National Earth System Science Data Center, Beijing 100101, China
5 Hebei Key Laboratory of Mining Development and Security Technology, Hebei Industrial Technology Institute of Mine Ecological Remediation, College of Mining Engineering, North China University of Science and Technology, Tangshan 063210, China; liumy917@ncst.edu.cn (M.L.); manwd@ncst.edu.cn (W.M.)
6 College of Tourism and Geographic Sciences, Jilin Normal University, Siping 136000, China; liujiafu@jlnu.edu.cn
* Correspondence: renchy@iga.ac.cn; Tel.: +86-0431-82536082

Abstract: Accurate and effective mapping of forest aboveground biomass (AGB) in heterogeneous mountainous regions is a huge challenge but an urgent demand for resource managements and carbon storage monitoring. Conventional studies have related the plot-measured or LiDAR-based biomass to remote sensing data using pixel-based approaches. The object-based relationship between AGB and multi-source data from LiDAR, multi-frequency radar, and optical sensors were insufficiently studied. It deserves the further exploration that maps forest AGB using the object-based approach and combines LiDAR data with multi-sensor images, which has the smaller uncertainty of positional discrepancy and local heterogeneity, in heterogeneous mountainous regions. To address the improvement of mapping accuracy, satellite LiDAR data from GEDI and ICESat-2, and images of ALOS-2 yearly mosaic L band SAR (Synthetic Aperture Radar), Sentinel-1 C band SAR, Sentinel-2 MSI, and ALOS-1 DSM were combined for pixel- and object-based forest AGB mapping in a vital heterogeneous mountainous forest. For the object-based approach, optimized objects during a multiresolution segmentation were acquired by the ESP (Estimation of the Scale Parameter) tool, and suitable predictors were selected using an algorithm named VSURF (Variable Selection Using Random Forests). The LiDAR variables at the footprint-level were extracted to connect field plots to the multi-sensor objects as a linear bridge. It was shown that forests' AGB values varied by elevations with a mean value of 142.58 Mg/ha, ranging from 12.61 to 514.28 Mg/ha. The north slope with the lowest elevation (<1100 m) had the largest mean AGB, while the smallest mean AGB was located in the south slope with the altitude above 2000 m. Using independent validation samples, it was indicated by the accuracy comparison that the object-based approach performed better on the precision with relative improvement based on root-mean-square errors (RI_{RMSE}) of 4.46%. The object-based approach also selected more optimized predictors and markedly decreased the prediction time than the pixel-based analysis. Canopy cover and height explained forest AGB with their effects on biomass varying according to the elevation. The elevation from DSM and variables involved in red-edge bands from MSI were the most contributive predictors in heterogeneous temperate forests. This study is a pioneering exploration of object-based AGB mapping by combining satellite data from LiDAR, MSI, and SAR, which offers an improved methodology for regional carbon mapping in the heterogeneous mountainous forests.

1. Introduction

Forests hold an estimated 85% of the global terrestrial biomass, and the majority was stocked in the aboveground [1,2]. As an essential functional parameter of terrestrial ecosystems and climate changes, forest aboveground biomass (AGB) takes charge of the carbon exchange between the land and atmosphere [3–5]. Thus, accurate and efficient mapping of forest AGB is a critical need for comprehending carbon cycles and planning science-based forest managements. In spite of substantial efforts on improving AGB mapping, the large uncertainty still remains in heterogeneous mountainous regions [6,7].

Measured tree height and diameter from harvested trees, and species-sensitive allometric growth equations are traditionally used to accurately evaluate forest AGB [8]. However, this method is disruptive and spatially limited [9]. It has become a cost-effective and spatiotemporal comparable way to produce wall-to-wall forest AGB maps by combining sample measurements and satellite remote sensing data [10,11]. Optical remote sensing techniques were applied to AGB estimation at the earliest owing to the characteristic reflectance related to chlorophyll and water contents as well as horizontal structures [12,13]. However, limited by a poor penetration capacity, optical sensor-based AGB estimation has severe problems of cloud cover and saturation [14,15]. Signals from active microwave sensors penetrate canopies with a certain thickness and generate particular vertical information by various frequency bands and polarizations [16]. Thereinto, SAR (Synthetic Aperture Radar) earns the reputation for directly retrieval forest AGB mapping by the water-cloud family of models [17,18]. Yearly mosaic images from ALOS series (ALOS-1/2) L band SAR are globally free-access observations and provide comprehensive information on the geometry of different parts of tree within a pixel, which is particularly helpful for forest AGB mapping [19,20], whereas radar sensors are yet subject to signal saturation in case of AGB values above 150 Mg/ha in heterogeneous mountainous forests [21,22]. Namely, combining multi-sensor images from optical and SAR remote sensing is essential to improve accuracy of AGB estimation. Global Sentinel series images from C band SAR and multispectral instrument (MSI) combining active and passive sensors have been served as frequently-used data sources to map forest AGB with publicly accessibility [23,24]. Topographic indices from digital terrain models reflect the locally hydrothermal condition and are common predictors of forest AGB [25]. Among these digital terrain models, the digital surface model (DSM) from ALOS-1 L band interferometric SAR (InSAR) has higher precision, so that it is useful to extract the indices for forest AGB prediction [26]. Although abundant efforts on improving forest AGB by combining optical and SAR images as well as digital terrain models under a point–polygon framework, i.e., link sampling plots to polygon-level remote sensing indices, the saturation problem is still obvious in mountainous heterogeneous forests. Light Detection and Ranging (LiDAR) provides three-dimension structure features and reduces the saturation problems, which improves the result accuracy of forest AGB modeling [27,28]. Airborne LiDAR data remain primarily for forest AGB estimation, while because of a lack of space continuity, they are yet supplementary for large-scale AGB mapping.

Satellite GEDI and ICESat-2 collect global photon counting LiDAR data, which have been processed to produce open-access land topography and vegetation variables for AGB estimation since April of 2019 and September of 2018, respectively [29–32]. Specifically, canopy cover with a linear linkage to diameter at breast height (DBH) and forest height directly related to tree height have contributed greatly to AGB mapping [29,33]. Restricted to the coverage, the application of LiDAR data on a full-cover AGB mapping at a finer resolution still faces hardships without an assistance from remote sensing images.

The above-mentioned remotely sensed data have been adopted to forest AGB mapping at various scales and each has pros and cons [15,34]. To advance spatiotemporally uniform AGB estimation, progress has been achieved by combining LiDAR data with remote sensing imagers [35–37]. Ground samples, LiDAR footprint data, and full-cover images are generally combined by a point-line-polygon framework and has yielded accurate AGB maps: modeling measured AGB points by LiDAR variables—then modeling LiDAR-based AGB by predictors from images [38,39]. The relationship between the LiDAR-based AGB and image predictors is mainly modeled based on a pixel size, while notable accuracy improvements were reported in object-based studies which shows some advantages such as the smaller uncertainty of positional discrepancy and local heterogeneity [9,40]. It is insufficiently studied how a pixel- or object-based mapping influences uncertainties of forest AGB estimation when integrating satellite LiDAR data with MSI and SAR images. Meanwhile, the roles of multi-sensor data including LiDAR, L and C bands SAR, and MSI on AGB estimation were insufficiently studied. Therefore, the development and comparison of pixel and object-based approaches by modeling relationships between forest AGB with multi-source data specifically for using datasets from GEDI, ICESat-2, ALOS, and Sentinel series facilitate the generation of finer-resolution accurate AGB maps.

This study aims to develop and compare pixel- and object-based mapping by integrating multi-sensor satellite data from LiDAR, SAR, and MSI to improve full-cover forest AGB estimation in a heterogeneous mountainous area. The Changbai Mountain National Nature Reserve (CMNNR) supports numerous endemic plant species and biodiversity of northeast Asia [41,42]. Taking this vital ecoregion with typical heterogeneous mountainous forests as the study area, the integration of GEDI and ICESat-2 data with images from ALOS and Sentinel series was conducted in this study. Specific goals were to: determine the relations of forest AGB to features from LiDAR, multi-frequency SAR, and MSI; compare pixel- and object-based AGB estimation by combining LiDAR data and images from SAR and MSI; and mapping forest AGB in mountainous heterogeneous forests.

2. Materials and Methods

2.1. The Study Area

Established in 1961, the CMNNR occupies an area of 195,852 ha with the latitude from 41°42′ to 42°25′ N and longitude from 127°42′ to 128°17′ E in Jilin Province, northeastern China (Figure 1). It is capped by the Tianchi, a crater lake, dividing the border of China and North Korea. This site was featured by significant vertical zonation of climate and vegetation. The mean annual precipitation is 700–1400 mm, and average annual temperature is −7 to 3 °C [43]. This area has the largest protected temperate forests covering 177,082 ha (90.4%), and are divided into core, buffer, and experimental functional management zones. The human disturbances are prevented in the core area, while eco-tourism and foundations for natural resource propagation are established in the experimental area [44]. From the foot to the peak of the CMNNR, vegetation distributions include forests of mixed broadleaf-conifer with altitudes below 1100 m, dark-coniferous spruce-fir with elevations from 1100 to 1700 m and Ermans birch (1700–2000 m), as well as alpine tundra [45].
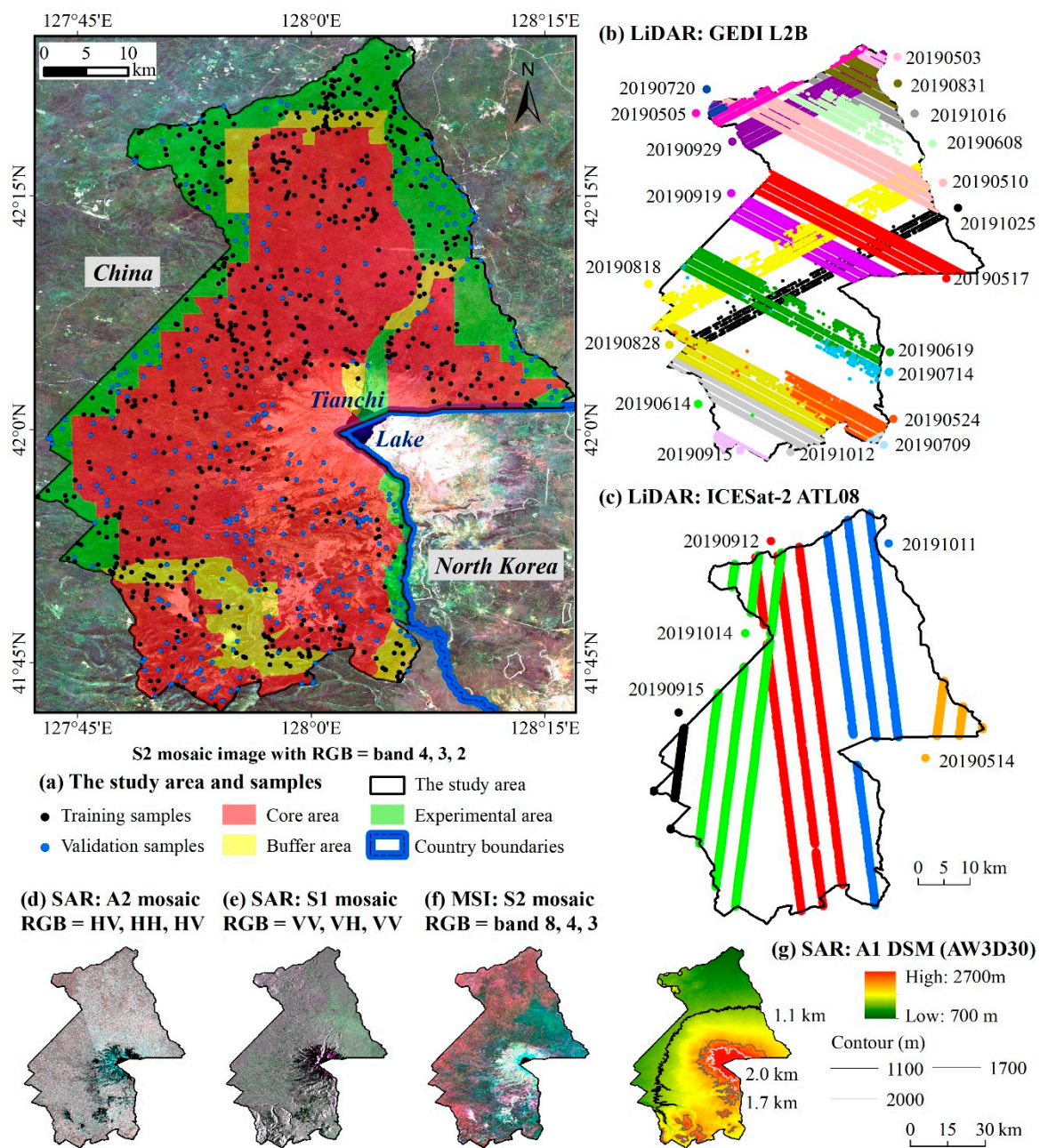
Figure 1. The CMNNR, field plots (**a**) and multi-sensor dataset of filtered GEDI LiDAR L2B products (**b**), ICEsat-2 LiDAR ATL08 products (**c**), a yearly mosaic image of 2019 from ALOS-2 SAR (Synthetic Aperture Radar) (A2) (**d**), mosaic images during May to October of 2019 from Sentinel-1 SAR (S1) (**e**), Sentinel-2MSI (S2) L2A (**f**), and ALOS-1 (A1) DSM data (AW3D30) (**g**).

2.2. Data

2.2.1. Field Data

The field measurements started from May to October of 2019 across the CMNNR, using a stratified sampling design, i.e., randomly generated samples by masking out non-forest areas, while the unavailable plots were substituted by the nearest homogeneous sites. A total of 1000 25 × 25 m samples were measured as shown in Figure 1a. Limited by the dense tree cover and poor labor, it has great uncertainty to measure tree height in the study area. Thus, field-observed point-level AGB was calculated by the measured DBH and allometric equations as listed in Table 1 [46]. Specifically, the observed value of forest AGB at a point was the biomass sum of trunks, branches, and leaves of all trees.

Table 1. The allometric growth equation for calculating forest aboveground biomass (AGB) by diameter at breast height (DBH).

Tree Species/Family/Types	Trunk	Branch	Leaf
Betula platyphylla Suk.	$0.1951 \times DBH^{2.2398}$	$0.0228 \times DBH^{2.2723}$	$0.0111 \times DBH^{1.9708}$
Tilia tuan Szyszyl.	$0.1286 \times DBH^{2.2255}$	$0.0445 \times DBH^{1.9516}$	$0.0197 \times DBH^{1.6667}$
Betula costata Trautv.	$0.1555 \times DBH^{2.2273}$	$0.0134 \times DBH^{2.4932}$	$0.0092 \times DBH^{2.0967}$
Populus L.	$0.2538 \times DBH^{1.1815}$	$0.0470 \times DBH^{1.9739}$	$0.0222 \times DBH^{2.1885}$
Ulmus pumila L.	$0.0971 \times DBH^{2.3253}$	$0.0278 \times DBH^{2.3540}$	$0.0239 \times DBH^{2.0051}$
Quercus L.	$0.1030 \times DBH^{2.2950}$	$0.0160 \times DBH^{2.6080}$	$0.0110 \times DBH^{2.2170}$
Pinus koraiensis Sieb. et Zucc.	$0.0418 \times DBH^{2.5919}$	$0.0208 \times DBH^{1.9612}$	$0.0873 \times DBH^{1.3480}$
Abies fabri (Mast.) Craib	$0.0543 \times DBH^{2.4242}$	$0.0255 \times DBH^{2.0726}$	$0.0773 \times DBH^{1.5761}$
Picea asperata Mast.	$0.0562 \times DBH^{2.4608}$	$0.1298 \times DBH^{1.8070}$	$0.1436 \times DBH^{1.6729}$
Pinus sylvestris var. *mongolica* Litv.	$0.1790 \times DBH^{2.0310}$	$0.0844 \times DBH^{1.7692}$	$0.0732 \times DBH^{1.6675}$
Larix gmelinii (Rupr.) Kuzen.	$0.0526 \times DBH^{2.5257}$	$0.0085 \times DBH^{2.4815}$	$0.0168 \times DBH^{2.0026}$
Other broad-leaved trees	$0.2266 \times DBH^{2.1699}$	$0.0121 \times DBH^{2.5685}$	$0.0229 \times DBH^{1.9485}$
Other coniferous trees	$0.0425 \times DBH^{2.5971}$	$0.0177 \times DBH^{2.0585}$	$0.0618 \times DBH^{1.4771}$

### 2.2.2. LiDAR Data and Pre-Processing

It was confirmed in previous research that LiDAR-estimated canopy cover and height had a generalized linear relationship with forest AGB as [27,47,48]. GEDI L2B data collected in accordance with the period of field campaign as listed in Table 2 were downloaded from Land Processes Distributed Active Archive Center, which were retrieved from the directional gap probability profile of original waveforms. Then, valid canopy cover and height (Figures 1b and 2) were extracted by the rGEDI R Package from downloaded L2B data [49,50]. Totally 35,819 pairs were obtained.

Table 2. The downloaded LiDAR dataset from GEDI and ICESat-2.

Source	Level	Spatial Resolution	Date	Elements
GEDI	2B	25 m	20190503, 0505, 0510, 0517, 0524, 0530, 0608. 0614, 0619, 0630, 0709, 0714, 0720, 0804, 0813, 0818, 0828, 0831, 0910, 0915, 0919, 0929, 1012, 1016, 1025	T1602, 2593, 1296, 1143, 2260, 5439, 1449, 4628, 2413, 0531, 4781, 3683, 3863, 1476, 4448, 4322, 3530, 0026, 0512, 3377, 2566, 1170, 0684, 4142, 2899
ICESat-2	ATL08	100 m	20190514, 0912, 0915, 1011, 1014	07040306, 11690402, 12070406, 02240502, 02620506

Limited by the coverage of GEDI products during the time phase of field samples, ICEsat-2 LiDAR data were also added with GEDI as a linear bridge to acquire substantial AGB training inputs for random forests (RF) modeling. Similarly, ICEsat-2 LiDAR ATL08 products from May to October of 2019 were downloaded from National Snow and Ice Data Center to extract canopy cover and height (Figures 1c and 2). The canopy height as h_canopy was the 98% height (RH98), retrieving from a cumulative distribution of all canopy photons within each 100 m laser footprint [51]. The canopy_openness was the standard deviation of photons classified as canopies within the segment [52]. In total, 6937 valid pairs were picked out from ICESat-2 ATL08 using the Python software.

The sampling sites within the coverage of the valid LiDAR data were set as training points (*n* = 670) to establish the pixel- and object-based models, while the remaining 330 samples were validation points for examining pixel- and object-based model performances (Figure 1).
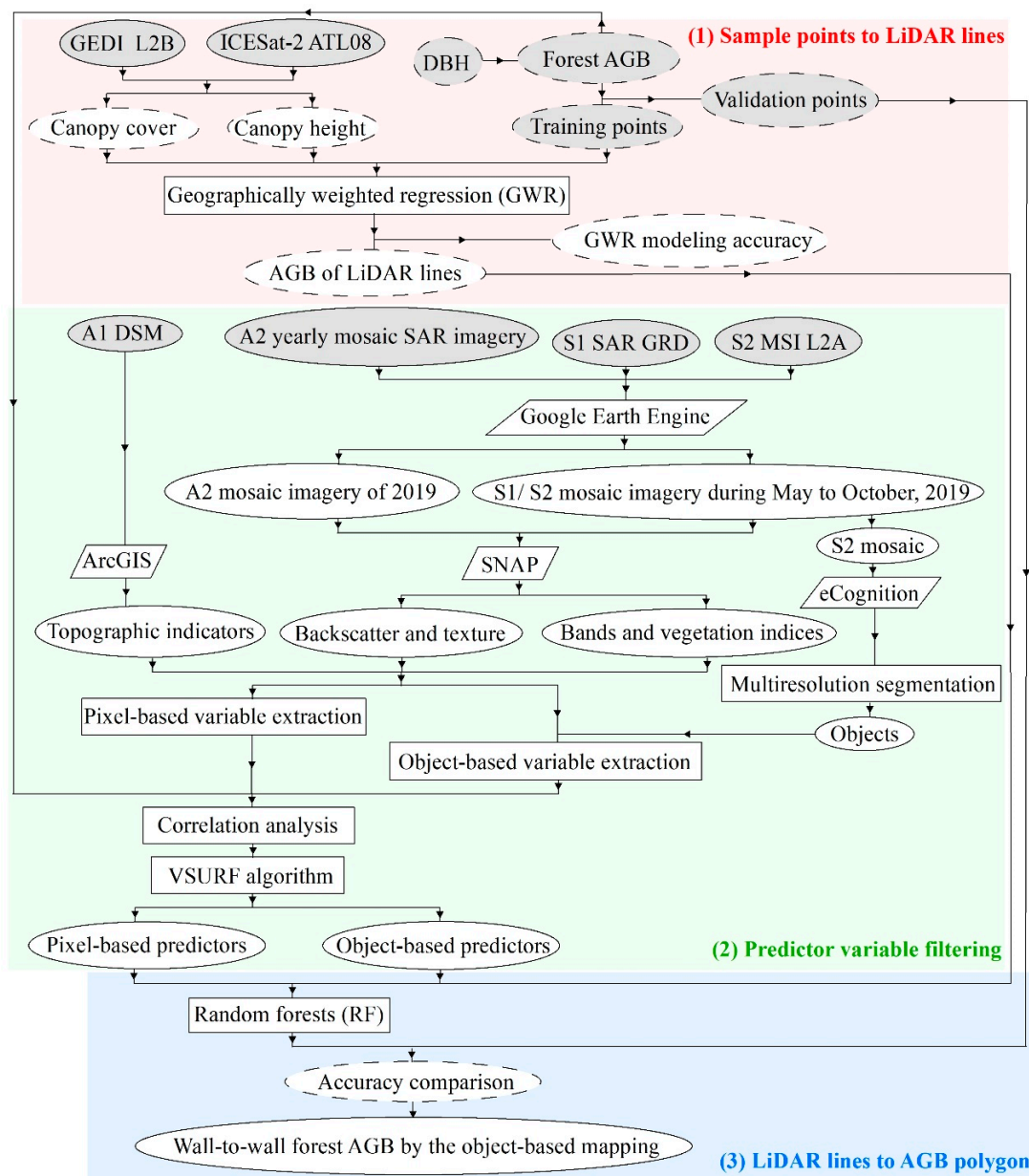
Figure 2. Overall workflow of object-based mapping of forest AGB by integrating LiDAR data with MSI and SAR images.

2.2.3. Optical and SAR Images and Pre-Processing

The adopted images from ALOS and Sentinel series were listed in Table 3. The mosaic images were pre-processed of topological corrections and acquired in the Google Earth Engine (GEE) platform (Figure 2). The ALOS-2 yearly mosaic images of 2019 (Figure 1d) were masked and converted to a normalized backscatter coefficient. In keeping with the period of field campaign, the mosaic images (Figure 1e) were produced from 47 Sentinel-1 C band SAR images by filtering, converting, and mosaicking [53]. Median values of multispectral bands of 219 Sentinel-2A L2A images were composited as the S2 mosaic (Figure 1f) after the cloud and noise removal [54]. To calculate topographic indicators, the DSM products from ALOS-1 (Figure 1g) were downloaded from the Japan Aerospace

Exploration Agency (Figure 2). All pre-processed remote sensing images were re-projected into the same projection and re-sampled into 10 m spatial resolution.

Table 3. The adopted images from A2, S1, S2, and A1 DSM.

Source	Level	Spatial Resolution	Date	Elements
A2	Yearly mosaic	25 m	2019	N42E127, N42E128, N43E127, N43E128
S1	Ground Range Detected (GRD) scenes	10 m	20190504, 0511, 0523, 0604, 0616, 0628, 0710, 0722, 0803, 0815, 0827, 0901, 0908, 0913, 0920, 1002, 1014, 1026	S1A_030CEC_4C1D, 3104D_C272, 315C5_F0B1, 31B36_F05C, 3207F_6155, 325B7_927A, 32B0B_9904, 33052_2FEE, 335A7_2036, 33B72_710E, 34189_6AF3, 34415_3340, 3479D_8BE2, 34A27_DC13, 34DA7_D875, 353AB_F55C, 359B8_7567, 35FB6_A688
			20190503, 0508, 0515, 0520, 0527, 0601, 0608, 0613, 0620, 0625, 0702, 0714, 0719, 0726, 0731, 0807, 0812, 0819, 0831, 0905, 0912, 0917, 0924, 0929, 1006, 1011, 1018, 1023, 1030	S1B_1E41C_F791, 1E671_C1F2, 1E9A3_E18A, 1EBD2_89DA, 1EEFF_9395, 1F128_5411, 1F438_AF2E, 1F65C_F904, 1F96F_3C04, 1FB87_96B7, 1FE9A_9303, 203C2_5BAE, 205CF_E75B, 208D7_5F71, 20B01_D973, 20E22_7E43, 2105F_D04A, 21398_0C46, 21909_5957, 21B40_2E33, 21E81_62C0, 220BA_841B, 223E8_0AF8, 2261D_DA49, 2296A_F309, 22B9B_574C, 22ECA_6BF5, 230F2_5472, 2343E_D938
S2	2A, orthorectified atmospherically corrected surface reflectance	10 m	20190503, 0506, 0513, 0516, 0518, 0523, 0526, 0602, 0605, 0612, 0615, 0622, 0625, 0702, 0705, 0712, 0715, 0722, 0725, 0801, 0804, 0811, 0814, 0821, 0824, 0831, 0903, 0910, 0913, 0920, 0923, 0930, 1003, 1010, 1013, 1020, 1023, 1030	There are three images on each date as S2A_T52TCM, T52TDM, and T52TDN.
			20190501, 0508, 0511, 0528, 0531, 0607, 0610, 0617, 0620, 0627, 0630, 0707, 0710, 0717, 0720, 0727, 0730, 0806, 0809, 0816, 0819, 0826, 0829, 0905, 0908, 0915, 0918, 0925, 0928, 1005, 1008, 1015, 1018, 1025, 1028	There are three images on each date as S2B_T52TCM, T52TDM, and T52TDN.
A1	DSM	30 m	Derived from A1 SAR data during 2006 to 2011	N41E127, N41E128, N42E127, N42E128

On the basis of related studies, 60 multi-sensor variables were chosen and calculated for AGB modeling, as listed in Table 4, with 4, 24, 26, and 6 indicators from A2, S1, S2,

and A1, respectively [13,55,56]. Texture features from S1, and normalized backscatter coefficients as well as their calculations from A2 and S1 were extracted from mosaic SAR images in SNAP software due to the sensitivity to tree structure and insensitivity to topography [23,56]. The reflectance and spectral indices from mosaic MSI images were calculated in SNAP software. Topographic indicators were calculated based on ALOS-1 DSM in ArcGIS software.

Table 4. Multi-sensor variables for AGB modeling.

Images	Variables		Description
A2 mosaic	Backscatter	HH	Normalized backscatter coefficient of horizontal transmit-horizontal channel in dB
		HV	Normalized backscatter coefficient of vertical transmit-vertical channel in dB
		RFDI	Radar forest degradation index, $(HH - HV)/(HH + HV)$
		V/H_L	HV/HH
S1 mosaic	Backscatter	VV	Normalized backscatter coefficient of vertical transmit-vertical channel in dB
		VH	Normalized backscatter coefficient of vertical transmit-horizontal channel in dB
		NP	Normalized polarization, $(VH - VV)/(VH + VV)$
		V/H_C	VV/VH
	Texture	VV/VH_CON	Contrast
		VV/VH_DIS	Dissimilarity
		VV/VH_HOM	Homogeneity
		VV/VH_ASM	Angular second moment
		VV/VH_ENE	Energy
		VV/VH_MAX	Maximum probability
		VV/VH_ENT	Entropy
		VV/VH_MEA	Gray-level co-occurrence matrix (GLCM) mean
		VV/VH_VAR	GLCM variance
		VV/VH_COR	GLCM correlation
S2 mosaic	Multispectral bands	B2	Blue, 490 nm
		B3	Green, 560 nm
		B4	Red, 665 nm
		B5	Red edge, 705 nm
		B6	Red edge, 749 nm
		B7	Red edge, 783 nm
		B8	Near infrared, 842 nm
		B8a	Near infrared, 865 nm
		B11	Short-wave infrared, 1610 nm
		B12	Short-wave infrared, 2190 nm
	Vegetation indices	RVI	Ratio vegetation index, B8/B4
		DVI	Difference vegetation index, $B8 - B4$
		NDVI	Normalized difference vegetation index, $(B8 - B4)/(B8 + B4)$
		EVI	Enhanced vegetation index, $2.5 \times (B8 - B4)/(B8 + 6 \times B4 - 7.5 \times B2 + 1)$
		S2REP	Sentinel-2 red-edge position index, $705 + 35 \times [(B4 + B7)/2 - B5] \times (B6 - B5)$
		REIP	Red-edge infection point index, $700 + 40 \times [(B4 + B7)/2 - B5]/(B6 - B5)$
		SAVI	Soil adjusted vegetation index, $1.5 \times (B8 - B4)/8 \times (B8 + B4 + 0.5)$
		MTCI	Meris terrestrial chlorophyll index, $(B6 - B5)/(B5 - B4)$
		MCARI	Modified chlorophyll absorption ratio index, $[(B5 - B4) - 0.2 \times (B5 - B3)] \times (B5 - B4)$

Table 4. *Cont.*

Images	Variables		Description
		NDVI45	Normalized difference vegetation index with bands 4 and 5, (B5 − B4)/(B5 + B4)
		NDVI56	Normalized difference vegetation index with bands 5 and 6, (B6 − B5)/(B6 + B5)
		NDVI57	Normalized difference vegetation index with bands 5 and 7, (B7 − B5)/(B7 + B5)
		NDVI58a	Normalized difference vegetation index with bands 5 and 8a, (B8a − B5)/(B8a + B5)
		NDVI67	Normalized difference vegetation index with bands 6 and 7, (B7 − B6)/(B7 + B6)
		NDVI68a	Normalized difference vegetation index with bands 6 and 8a, (B8a − B6)/(B8a + B6)
		NDVI78a	Normalized difference vegetation index with bands 7 and 8a, (B8a − B7)/(B8a + B7)
DSM	Topographic indicators	H	Elevation
		β	Slope
		A	Aspect
		M	Surface roughness, 1/cosβ
		TWI	Topographic wetness index, Ln [Ac/tanβ], Ac is the catchment area directed to the vertical flow
		SPI	Stream power index, Ln [Ac × tanβ × 100]

2.3. Methods

To improve the estimation of forest AGB by a comparison on pixel- and object-based mapping based on LiDAR data and images from MSI and SAR, the workflow contains three major sections as follows (Figure 2). Indeed, the pixel- and object-based approaches were just different in the variable extraction and mapping units. In the object-based approach, multi-sensor variable values were calculated as the mean values within optimal objects, and the final mapping unit was also the object. While in the pixel-based approach, values of multi-sensor variables and predicted AGB were the exact values within the pixel.

2.3.1. Estimation of AGB Lines from GEDI and ICESAT-2 Data by GWR

Studies had shown that forest AGB was linearly explained by LiDAR-estimated canopy cover and height to a large extent [38,57,58], but their generally linear relationship varied by location. Hence, this study adopted geographically weighted regression (GWR) to estimate AGB from LiDAR lines (Figure 3).
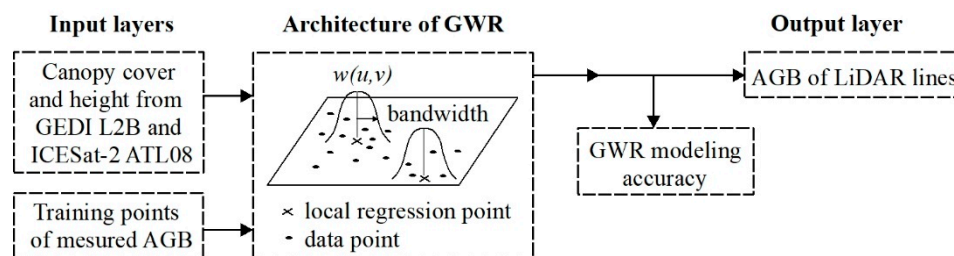

Figure 3. Illustration of AGB estimation from LiDAR lines by geographically weighted regression (GWR) modeling. W(u, v), a weight matrix, ensures measurements obeying a distance decay.

Relied on the locally smooth idea, GWR simulated local relationships of forest AGB with LiDAR-estimated canopy cover and height by individually calculating parameters that obeyed a distance decay [59,60]. Namely, the greater weight was assigned when the location of a measurement was closer [61]. The least squares method weighted by locations of field-measured AGB was used [62]. A GWR model was established for LiDAR-based AGB using GWR4 software and training samples by quantifying parameters, i.e., model

type, kernel of Gaussian or bi-square types, fixed or adaptive bandwidth selection method and criteria [63,64].

2.3.2. Filtering Predictors Based on Pixel- or Object-Based Analysis

Pixel- and object-based correlation analysis were tested, respectively, and then compared with each other. For a pixel-based analysis, the variable was extracted at the locations of field-measured AGB plots. In the object-based process, the variable value was the average within the object that related to a plot-level AGB. To acquire the objects, the multiresolution segmentation algorithm on the eCognition software was applied by setting three parameters of shape as 0.1, compactness as 0.5, and scale to control the shape, size, and spectral variation of a segmented S2 mosaic image with all multispectral bands (Figure 2) [40,65]. The suitable scale parameter was estimated by ESP (Estimation of the Scale Parameter) tool, and the first steep peak of the ROC curve in Figure 4 corresponding to a scale level of 45 was set for the segmentation [66]. Finally, the study area was segmented into 147,108 objects.
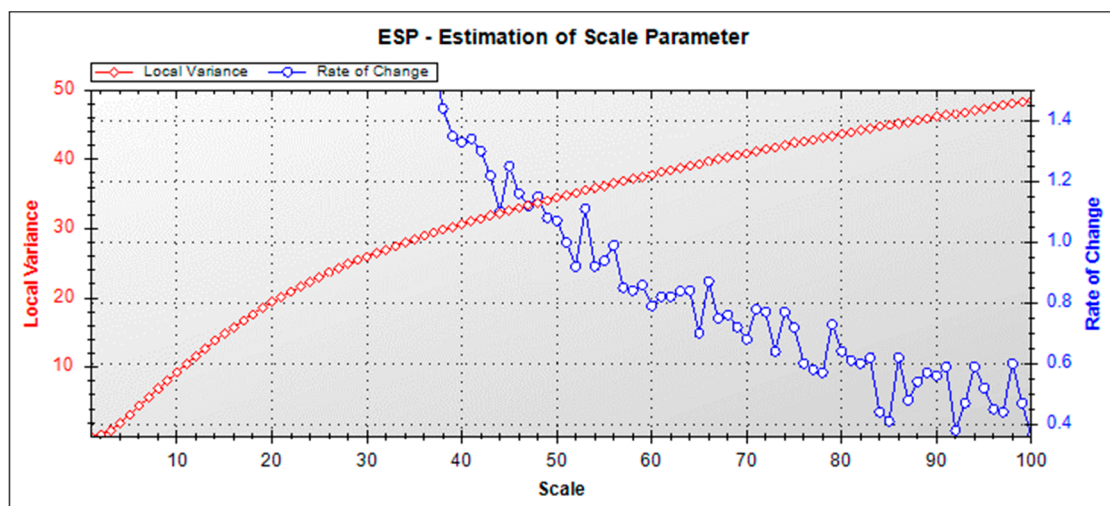

Figure 4. Local variance and rate of change of different values of scale calculated by the ESP tool with a shape of 0.1 and compactness of 0.5.

Pairwise Pearson's correlation analysis in SPSS software was conducted to determine predictor variables for AGB estimation and the candidate was selected as the significantly related variables ($p < 0.05$). The VSURF (Variable Selection Using Random Forests) algorithm gained fame for optimized variable selection [67]. By mean variable importance values of random forest modeling, the VSURF algorithm filtered out unconsidered predictors. After that, the most suitable variables were selected by an iterative optimization for field-measured AGB prediction to fit the model with a high possibility [68]. The VSURF package of R software was used to filter the candidate for the optimized predictor variables for prediction accuracy of forest AGB.

2.3.3. Mapping AGB Polygons from AGB Lines and Multi-Sensor Predictors by Random Forests

RF was less sensitive to noise in training samples and had extensive improved applications on remote sensing-based AGB mapping [15,38,69]. An RF model was determined by two parameters as the number of features to split nodes and number of trees for optimization [56]. Calculating the mean variance decrease, the variable importance of a RF model was identified [70]. Two units of predictors were imported in WEKA software as shown in Figure 5 for the pixel- and object-based RF modeling, respectively, and the accuracy comparison was made according to the 330 independent validation points by calculating root-mean-square errors (RMSE), mean errors (ME), coefficient of determination (R^2), and

the relative improvement (RI) [56]. Predicted AGB estimation was the mean of all trees. The wall-to-wall forest AGB was illustrated by the object-based RF modeling.
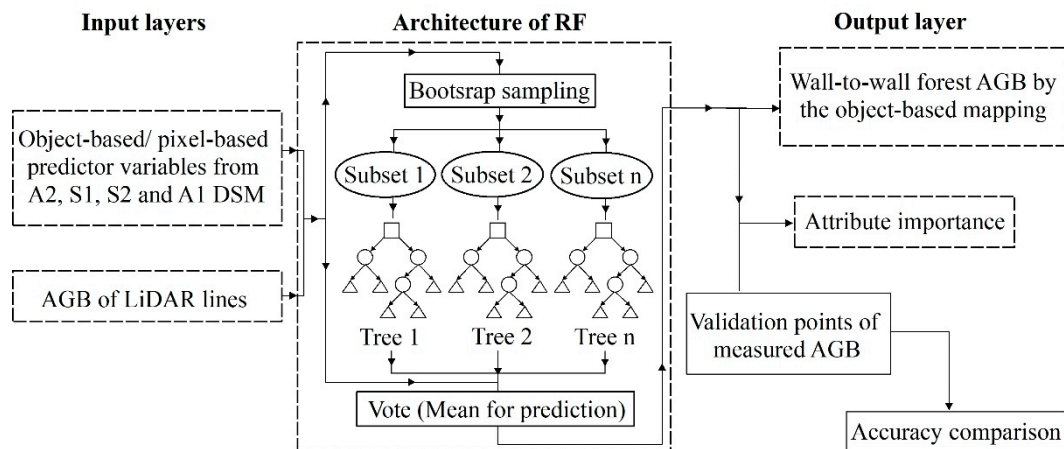

Figure 5. Delineation of random forests (RF) mapping of forest AGB based on LiDAR lines and multi-sensor images.

3. Results

3.1. The GWR Model and LiDAR-Based AGB Lines

The measured forest AGB values were between 0.46 and 686.13 Mg/ha with the majority below 250 Mg/ha (Figure 6a). For visual display, the accuracy of the final AGB map, the measured values were split into five levels with the same frequency (Figure 6a). The mean was 152.62 Mg/ha and the median was 88.59 Mg/ha with the standard deviation (SD) value of 152.18 Mg/ha (Figure 6b). Along three vertical vegetation zones, the mean AGB values increased to the peak of 102.45 Mg/ha in the mixed coniferous and broad-leaved forests (<1100 m), and then decreased to the bottom of 74.16 Mg/ha in Ermans birch forest (1700–2000 m).
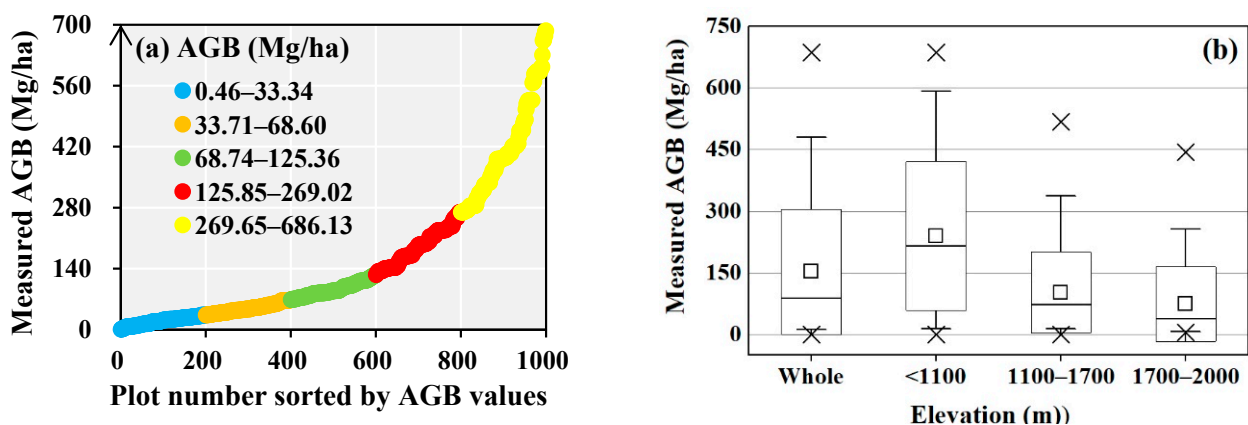

Figure 6. The AGB profiles of forest measured samples from Plot 1 to 1000 (**a**) and value distribution along different altitudinal gradients (**b**). The boxes denote values within the range of the mean ± standard deviation (SD), lines in boxes are medians, and squares depict means with the dash as the whisker of 5–95%, as well as crosses as the minimum and maximum values.

The canopy cover from GEDI and ICESat-2 ranged from 0.002 to 11.61, the values above 1 were belonging to ICESat-2 products, as the SD of classified canopy photons (Table 5). The canopy height from GEDI and ICESat-2 was 1.76 to 45.91 m. Based on canopy cover and height from GEDI and ICESat-2 as well as training samples of measured AGB, the GWR model was built by a Gaussian approach and a fixed Gaussian kernel as the weight

function with the smaller RMSE value of 38.64 Mg/ha compared to adaptive bandwidth. The golden selection method and small sample bias corrected Akaike information criterion (AICc) determined the optimal bandwidth as 104.33. The AGB values extracted from GWR modeling based on 42,756 pairs of canopy cover and height ranged from 0.39 to 684.09 Mg/ha. The median of LiDAR-based AGB was 151.48 Mg/ha, and, for SD values, it was 117.99 Mg/ha (Table 5).

Table 5. Statistical descriptions of the LiDAR-derived canopy cover (C) and height (H_t) as well as AGB.

Variables	Minimum	Maximum	Mean	Medium	SD
C	0.002	11.61	1.78	0.61	2.68
H_t (m)	1.76	45.91	22.84	24.45	7.55
AGB (Mg/ha)	0.39	684.09	179.50	151.48	117.99

3.2. Predictor Variables

In the object-based process, 47 variables had significant correlations with measured forest AGB (Table 6), as four from L band SAR, 15 from C band SAR, 24 from MSI, and four from DSM. However, HV from A2, VV_DIS, and VH_DIS from S1, A, and TWI from DSM did not correlate significantly with AGB in the pixel-based process. With forest AGB increasing, variables from the pixel- and object-based processes had the same trend. Overall, remote sensing indices were better connected to AGB in the object-based process with the larger *r* values than the pixel-based analysis.

Normalized backscatter coefficients from L band SAR images had strongly significant relation to measured AGB, while that from C band SAR images had a weaker correlation without the significance. The calculation of backscatters from A2 was unhelpful to enhance the r values, especially for an object-based process, whereas the texture analysis was helpful with heightening the correlation of backscatters from S1 to AGB. The texture characteristics of VV backscatters were more related to AGB than that of the VH channel. In the object-based process, HV backscatters from A2 had the stronger relationship than HH backscatters, which was in contrasted with the pixel-based process. S1 texture features from the pixel- and object-based processes had similar relationships with AGB.

All variables from MSI were significantly correlated with AGB. Vegetation indices had stronger correlation to AGB than original band reflectance, especially the variables involved in red-edge bands. The top five of the object-based correlation were MTCI, REIP, NDVI57, NDVI56, and NDVI67, while that of the pixel-based relevant were NDVI57, NDVI56, NDVI58a, REIP, and MTCI. Elevation from A1 DSM showed the strongest relation to AGB among all remote sensing indices. The calculation of slope, e.g., M and TWI, was helpful with increasing the correlation than the original indicators. The indicator from the hydrologic process, TWI, was strongly related to AGB in the object-based analysis but did not show the significance in the pixel-based analysis.

Both in the pixel- and object-based processes, the elevation from DSM and variables involved in red-edge bands from MSI displayed the maximum correlation, and impacts of backscatters from C band SAR as well as their calculation were marginal. The correlation of variables from L band SAR was at the average level.

After preliminary elimination and ranking, by the VSUPF trees fixed to 500 and features as the variable number/3 [67], the predictor variables were selected. In the pixel-based process, eight predictors were chosen with the lowest out-of-bag (OOB) error, as marked "Yes" in Table 6, including VV_MEA, VV_COR, VH_COR, VH_HOM, B5, EVI, NDVI58a, and H. As for the object-based analysis, 10 predictors were selected, i.e., HV, VV_MEA, EVI, MTCI, NDVI45, NDVI56, NDVI57, NDVI78a, H, and TWI. On the whole, the object-based analysis mainly selected vegetation indices that involved red-edge bands from S2 MSI, but the pixel-based process chose texture features from C band SAR.

Table 6. The filtering result of predictor variables from remote sensing indices which were significantly related to measured AGB with a mark * as the *p*-value of the *t*-test being below 0.05 and ** as a *p*-value below 0.01.

Images	Variables	*r*		VSURF-Selected Predictors	
		Pixel-Based	Object-Based	Pixel-Based	Object-Based
A2 mosaic	HH	0.12 **	0.11 **	No	No
	HV		0.17 **		Yes
	RFDI	−0.08 *	−0.12 **	No	No
	V/H_L	0.09 **	0.13 **	No	No
S1 mosaic	VV_DIS		0.08 *		No
	VV_HOM	−0.15 **	−0.17 **	No	No
	VV_ASM	−0.11 **	−0.11 **	No	No
	VV_ENE	−0.14 **	−0.15 **	No	No
	VV_MAX	−0.13 **	−0.14 **	No	No
	VV_ENT	0.15 **	0.17 **	No	No
	VV_MEA	0.11 **	0.11 **	Yes	Yes
	VV_COR	0.17 **	0.19 **	Yes	No
	VH_DIS		0.06 *		No
	VH_HOM	−0.14 **	−0.16 **	Yes	No
	VH_ASM	−0.11 **	−0.11 **	No	No
	VH_ENE	−0.13 **	−0.14 **	No	No
	VH_MAX	−0.13 **	−0.14 **	No	No
	VH_ENT	0.14 **	0.16 **	No	No
	VH_COR	0.11 **	0.13 **	Yes	No
S2 mosaic	B2	−0.11 **	−0.10 **	No	No
	B3	−0.16 **	−0.17 **	No	No
	B4	−0.17 **	−0.17 **	No	No
	B5	−0.15 **	−0.15 **	Yes	No
	B6	0.08 *	0.09 **	No	No
	B7	0.11 **	0.13 **	No	No
	B8	0.09 **	0.10 **	No	No
	B8a	0.09 **	0.10 **	No	No
	RVI	0.23 **	0.25 **	No	No
	DVI	0.13 **	0.15 **	No	No
	NDVI	0.20 **	0.21 **	No	No
	EVI	0.15 **	0.17 **	Yes	Yes
	S2REP	0.21 **	0.23 **	No	No
	REIP	0.26 **	0.30 **	No	No
	SAVI	0.08 **	0.10 **	No	No
	MTCI	0.25 **	0.30 **	No	Yes
	MCARI	0.11 **	0.12 **	No	No
	NDVI45	0.12 **	0.13 **	No	Yes
	NDVI56	0.26 **	0.30 **	No	Yes
	NDVI57	0.27 **	0.29 **	No	Yes
	NDVI58a	0.26 **	0.27 **	Yes	No
	NDVI67	0.22 **	0.29 **	No	No
	NDVI68a	0.09 **	0.07 *	No	No
	NDVI78a	0.15 **	0.28 **	No	Yes
DSM	H	−0.43 **	−0.43 **	Yes	Yes
	A		−0.11 **		No
	M	0.16 **	0.21 **	No	No
	TWI		0.22 **		Yes

3.3. Forest AGB in the CMNNR Mapped by RF Models

According to the smallest RMSE values, 500 trees and five features were set to build the pixel-based RF model. Similarly, 500 trees and four features were set to build the object-based RF model. The results showed that predictors ranked by the attribute importance of

the pixel-based RF model were H, NDVI58a, VV_COR, EVI, B5, VV_MEA, VH_COR, and VH_HOM. Predictors sorted by the attribute importance of the object-based RF model were H, NDVI57, NDVI56, NDVI78a, TWI, NDVI45, VV_MEA, EVI, HV, and MTCI. Overall, the elevation, variables involved in red-edge bands, and texture features from VV backscatters were the most important predictors in RF modeling.

Table 7 showed the accuracy of pixel- and object-based RF models based on 330 validation samples. For further evaluating and comparing accuracy with related studies, the mean value of measured AGB was used to divide the ME and RMSE. ME values denoted that both approaches overestimated forest AGB. The accuracy demonstrated that the object-based approach outperformed pixel-based modeling (Figure 7). The object-based modeling reduced RMSE values by 4.46% and improved accuracy of AGB modeling with a *p*-value of the *t*-test below 0.01.

Table 7. Accuracy comparison between pixel- and object-based approach for RF modeling by independent validation data.

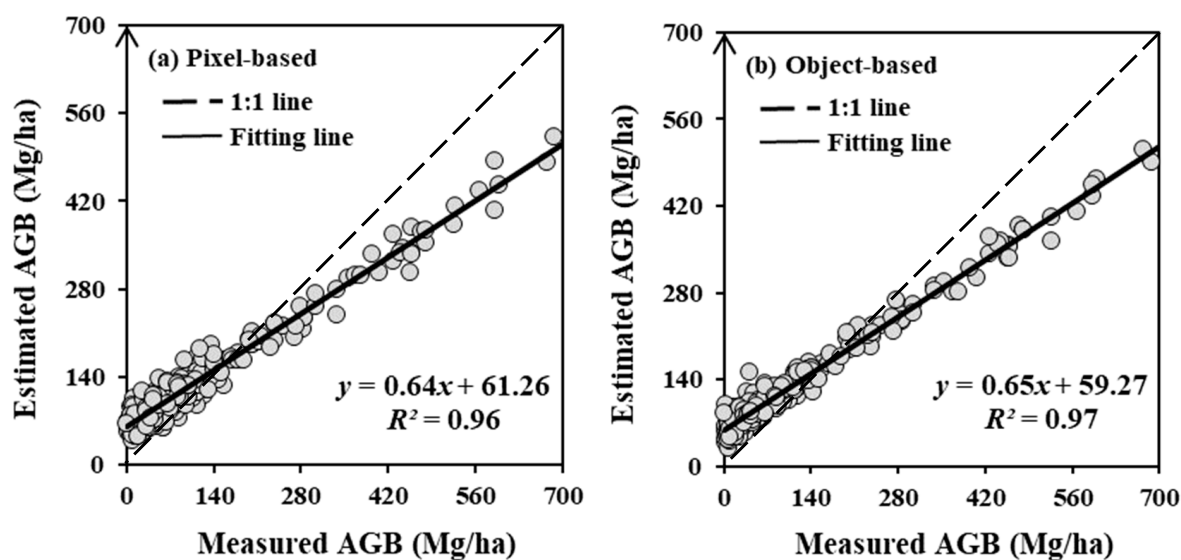| Modeling Approach	ME		RMSE		R^2	RI_{RMSE} (%)
	Mg/ha	%	Mg/ha	%		
Pixel-based	−24.22	−15.87	54.47	35.69	0.96	0
Object-based	−23.44	−15.36	52.04	34.10	0.97	4.46

Figure 7. Scatter diagrams of estimated AGB versus measured values.

Then, AGB distribution was mapped by abovementioned RF models. The object-based approach decreased mapping time by requiring less outputs of the RF prediction. The number of outputs in a pixel-based RF model was the number of all pixels, which was nearly 200,000, while that in an object-based was 147,108. The object-based RF mapping of forest AGB was as in Figure 8a. The mapped values were displayed at five levels on the same frequency of field-measured AGB as shown in Figure 6a. Mapped values had similar distributions and were close to the field-measured AGB, which was depicted by the same pattern at each level. By integrating LiDAR data with multi-sensor images and object-based RF modeling, estimated values of forest AGB were between 12.61 and 514.28 Mg/ha, with a mean of 142.58 Mg/ha and SD values as 90.21 Mg/ha (Figure 8b).
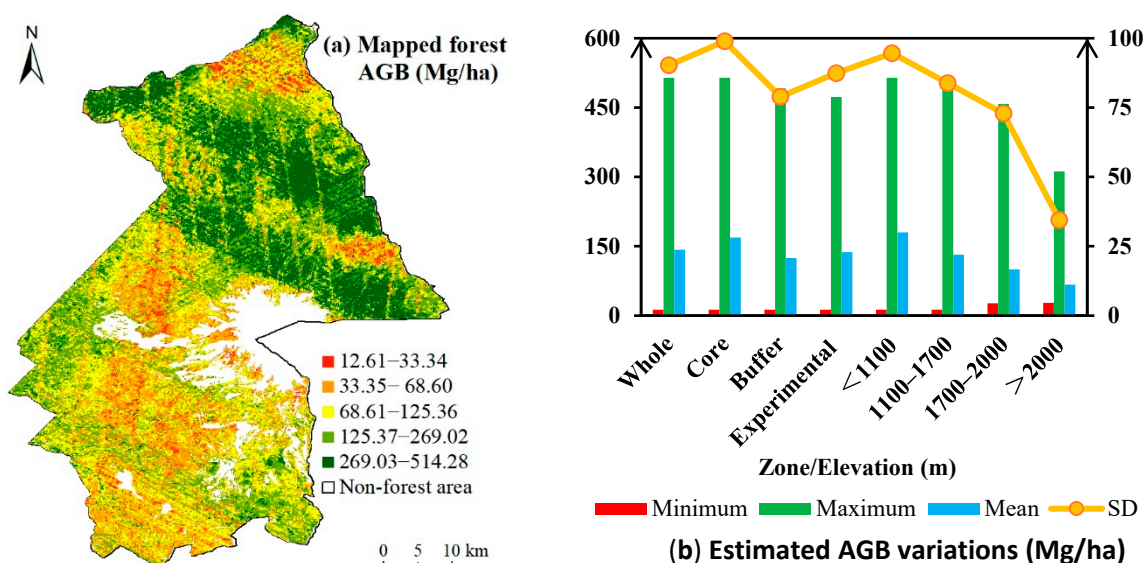
Figure 8. The spatial distribution of estimated forest AGB (**a**) and the estimated AGB variations of different elevation gradients and management zones (**b**) using object-based RF modeling.

The north slope with the lowest elevation (<1100 m) had the largest mean value of 179.72 Mg/ha, with AGB values ranging from 12.61 to 514.28 Mg/ha (Figure 8). In the south slope of the CMNNR with the altitude above 2000 m, the smallest mean value was 67.04 Mg/ha and AGB values were between 27.71 and 311.81 Mg/ha. Generally, the distribution of mapped values was approximate to the measured forest AGB (Figures 6b and 8b). The errors mainly generated by overestimations of small values (<68.60 Mg/ha) in the high-altitude (≥1700 m) area and underestimations of large AGB (>269.02 Mg/ha) in the low-elevation region. The core forests had the largest mean value of AGB as 168.75 Mg/ha, and that in buffer and experimental areas had approximate mean values as 124.63 and 137.41 Mg/ha, respectively.

4. Discussion

4.1. Pixel- versus Object-Based RF Modeling

The pixel- and object-based approaches mainly differed in variable extraction and the mapping unit. The variable filtered in the object-based approach was more consistent with previous studies than the pixel-based results (Table 6): indeed, in Table 6, the object-based *r* values demonstrated that HV backscatters were more sensitive to AGB than HH channel, and vegetation indices involved red-edge bands from S2 MSI had greater influence than texture features from S1 [56,71–73]. The object-based approach markedly decreased the prediction time, which merged homogeneous pixels into objects as the mapping unit. The assessment result of the object-based approach had higher accuracy than that of the pixel-based model (Table 7 and Figure 7). These comparisons revealed that the object-based approach improved forest AGB mapping by modeling the relationship at an object scale.

The RMSE values of estimation by the pixel- and object-based approach were 35.69% and 34.10%, respectively, which were smaller than the most published regional maps of forest AGB using similar methods as RMSE values from 21% to 67% [40,74]. This can be explained by the advantages of integrating multi-sensor data, especially GEDI and ICESat-2 products, and higher resolution of Sentinel series. It implied that the integration of GEDI and ICESat-2 LiDAR data and series images from ALOS and Sentinel was suitable for large-scale forest AGB mapping. This improvement was possibly because AGB lines extracted from LiDAR data reduced the saturation problem and heterogeneity, better matching the predictors from multi-sensor images [54]. However, the RI values as listed in Table 7 demonstrated that the improvement of the object-based modeling in this study was less than the previous study which directly link field-measured AGB and image objects [40]. This

inferred that the object-based modeling was more helpful to the traditional point–polygon approach than the point–line–polygon framework. It also meant that the integration of LiDAR data reduced known uncertainties related to the positional discrepancy between field data and imagery objects. Due to the coarser spatiotemporal resolution of LiDAR data than satellite images, it was difficult and had the large uncertainty to integrate all sensors using multi-sensor data fusion approach for AGB mapping [75], whereas the final object-based AGB map as Figure 8a by integrating LiDAR data with satellite images was patchy and striping. Namely, the progress of algorithms on AGB extraction from LiDAR lines and suitable segmented objects were crucial in future studies for a better linkage between measured points and imagery objects.

This study concluded that the object-based mapping of forest AGB by the integration of GEDI and ICESat-2 LiDAR data with MSI and SAR images was a promising methodology. It should be emphasized that AGB lines extraction from LiDAR data and segmented objects were crucial for improving the precision.

4.2. Contributions of Multi-Sensor Variables to AGB Modeling

The location-specific coefficient values of canopy cover and height denoted the contributions of LiDAR variables to AGB modeling (Figure 9), which was firstly revealed by this study. According to results of the GWR modeling, absolute values of most canopy cover coefficients were larger. This revealed that spatial variations of forest AGB were more susceptible to canopy cover from LiDAR, especially in the low altitude experimental zones of the north slope of the CMNNR. In general, absolute values of cover canopy coefficients decreased by the increasing altitude, and the trend of canopy height was opposite. This may be resulted from forest changes in vertical zones along elevation gradients. In fact, the greater influence of canopy height on AGB accumulation with the increasing elevation was owing to decreasing tree density and dominating coniferous forests in the CMNNR [41,43].
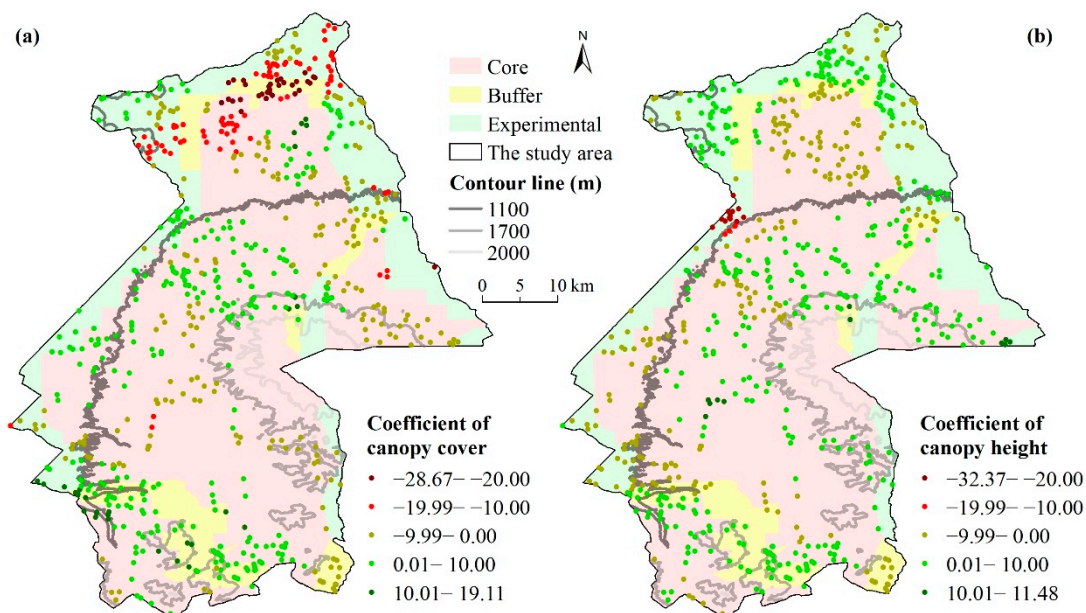

Figure 9. The location-specific coefficients of (**a**) canopy cover and (**b**) canopy height in the GWR model.

The role of MSI and SAR variables on AGB modeling was indicated by correlation coefficients (Table 6) and the attribute importance of RF models. The elevation was a proxy of InSAR height and was of prime importance on AGB mapping in the CMNNR. Meanwhile, agreed with relevant studies on Changbai flora regions [56,76], forest AGB of the CMNNR showed spatial variations along elevation gradients (Figures 6 and 8). The forests AGB in the southeastern part had greater spatial variations because of relatively

large elevation as well as its dramatic changes (Figures 1g and 8a). Due to a finer resolution in this highly heterogeneous landscape and drastic changes in altitude, the larger spatial variations of forest AGB compared to studies on nearby regions were shown [42,76]. This decreasing of forest AGB with increasing elevation was mainly because the reduction of moisture, temperature, and species richness, which affected biomass sequestration, changed remarkably along elevation gradients in the Changbai Mountain regions [77–79].

Sentinel-2 variables were powerful in vegetation type classification and horizontal structure retrieval such as estimations of canopy cover and DBH, especially the red-edge band indices reflecting chlorophyll contents [13,24,80]. Backscatters from SAR sensors were related to roughness and water content of vegetation [15,56]. Moreover, canopy cover estimated by MSI vegetation indices and backscatters from SAR were typical inputs in water-cloud models for AGB mapping [13,17]. However, subject to a coarse spatiotemporal resolution of ALOS-2 and the saturation problem of Sentinel-1 [81], the influence of backscatters from these SAR sensors on AGB mapping was marginal in this study compare with MSI variables. Texture features of Sentinel-1 images were more beneficial to AGB modeling than raw backscatters, particularly that of VV channel as shown in Table 6, owing to reducing impacts from the heterogeneity by textural analysis [56,82].

The comparison of roles of variables from four sources in AGB estimation revealed that LiDAR data outperformed images from other sensors ($RMSE_{LiDAR-lines}$ = 38.64 Mg/ha, $RMSE_{traditional}$ = 52.04 Mg/ha). This was because LiDAR directly measured the vegetation distribution along the vertical axis, which was sensitive to density variables as the most critical drivers of AGB increments [2,83]. These characteristics also caused a larger saturation value of LiDAR signals for precise assessment of biomass. Nevertheless, a coarse spatiotemporal resolution of LiDAR data results in a lack of coverage in the same phenological phase (Figure 1b,c), and it is also the reason that multi-sensor images were integrated.

In short, canopy cover and height from GEDI and ICESat-2 LiDAR, elevation from ALOS-1 DSM, and vegetation indices of red-edge bands from Sentinel-2 were recommended for large-scale AGB mapping in heterogeneous forests.

4.3. Uncertainty and Management in a Heterogeneous Mountain Landscape

The uncertainty is a crucial topic associated with remote sensing-based AGB, and was derived from field measurements, measured biomass calculation, predictors variables, and prediction algorithm [38,84]. In order to reduce the uncertainty, on-site measurements of tree height were abandoned and up-to-date allometric growth equations based on DBH values were adopted (Table 1).

The uncertainty of multi-source predictor variables was lessened by approximate acquisition time among multi-sensor variables and with on-site measurements. Substantial variables articulated in previous papers (Table 3) were calculated and filtered by VSURF tool to find optimized predictors. The sampling size matched the spatial resolution of GEDI products but was inconsistent with the ICESat-2 and multi-sensor data. The suitable sampling size would be explored further.

The modeling uncertainty was also considered. In the GWR modeling, three group of LiDAR variables were input, and the results were compared as Table 8. In other words, with the smallest RMSE values, GEDI and ICESat-2 products were combined in GWR modeling. The uncertainty of object-based modeling was also discussed as the predicted error in Part 4.2. The uncertainties related to the positional discrepancy and local heterogeneity were reduced by the OBA approach and taking LiDAR data as a linear bridge. It can be upgraded by suitable segmented objects and compared multiple algorithms.

Table 8. The comparison among GWR models based on three data sources.

Variable Source	Bandwidth	AICc	RMSE (Mg/ha)
GEDI	158.67	6560.47	41.67
ICESat-2	147.84	1630.92	56.75
Both	104.33	8099.31	38.64

On the whole, the uncertainty is still a huge challenge for forest AGB mapping in a heterogeneous mountain landscape. It is limited by on-site measurements, the spatiotemporal discrepancy of multi-source data, variable selection, and modeling algorithms. There is a great demand for the further exploration of suitable sampling sizes and modeling algorithms for reducing the uncertainty.

For the sustainable forestry, certain managements should be implemented according to the forest AGB map as well as coefficients of canopy cover and height (Figures 8 and 9). It was showed that canopy cover positively contributed to forest AGB in the low altitude experimental zones of the northwest slope of the CMNNR. This indicated that these forests with high stand density should be thinned to increase space and resources. It was urgent for forests on the south slope of the CMNNR to be enclosed for cultivation. Experimental forests should be felled for increment. Overall, the core zone was well-protected, while buffer and experimental areas need more attention.

5. Conclusions

To improve wall-to-wall forest AGB estimation in heterogeneous mountainous forests, this study developed a pioneering object-based approach by integrating GEDI and ICESat-2 data with images from Sentinel and ALOS series. This promising methodology was conducted in a vital ecoregion, the CMNNR in Northeast China, and efficiently acquired an AGB map of heterogeneous forests across elevation gradients, with the relative RMSE values of 34.10%. As the first exploration of object-based mapping of forest AGB by the integration of satellite LiDAR data from GEDI and ICESat-2 with series images of ALOS and Sentinel, this study provided an improved methodology on regional carbon mapping to support decision makers for the suitable management of the CMNNR.

According to the results, the following was concluded in this study:

(1) The object-based approach accurately mapped AGB of heterogeneous forests in the CMNNR, and improved accuracy of 4.46% compared to the pixel-based process. The object-based approach also selected more optimized predictors and markedly decreased the prediction time compared to the pixel-based analysis.

(2) Canopy cover and height explained forest AGB to a large extent (RMSE = 25.32%), and their effects on biomass varied by the elevation. The elevation from DSM and variables involved in red-edge bands from MSI were the most contributive predictors, and impacts of backscatters from C band SAR as well as their calculation were marginal.

(3) The map illustrated that forest AGB of CMNNR varied along elevation gradients, with values from 12.61 to 514.28 Mg/ha. The north slope of the CMNNR with the lowest elevation (<1100 m) had the largest mean value, while forests in the south slope with the altitude above 2000 m had the smallest mean AGB. Forests in core areas had a much larger mean value of AGB than that in buffer and experimental zones.

References

1. Lucas, R.M.; Mitchell, A.L.; Armston, J. Measurement of forest above-ground biomass using active and passive remote sensing at large (subnational to global) scales. *Curr. For. Rep.* **2015**, *1*, 162–177. [CrossRef]
2. Yue, Q.; Hao, M.; Li, X.; Zhang, C.; von Gadow, K.; Zhao, X. Assessing biotic and abiotic effects on forest productivity in three temperate forests. *Ecol. Evol.* **2020**, *10*, 7887–7900. [CrossRef] [PubMed]
3. Canadell, J.G.; Le Quéré, C.; Raupach, M.R.; Field, C.B.; Buitenhuis, E.T.; Ciais, P.; Conway, T.J.; Gillett, N.P.; Houghton, R.A.; Marland, G. Contributions to accelerating atmospheric CO_2 growth from economic activity, carbon intensity, and efficiency of natural sinks. *Proc. Natl. Acad. Sci. USA* **2007**, *104*, 18866. [CrossRef] [PubMed]
4. FAO. The State of the World's Forests 2018—Forest Pathways to Sustainable Development. 2018. Rome. License: CC BY-NC-SA 3.0 IGO. Available online: http://www.fao.org/3/I9535EN/i9535en.pdf (accessed on 15 August 2019).
5. Koju, U.A.; Zhang, J.; Maharjan, S.; Zhang, S.; Bai, Y.; Vijayakumar, D.B.I.P.; Yao, F. A two-scale approach for estimating forest aboveground biomass with optical remote sensing images in a subtropical forest of Nepal. *J. For. Res.* **2019**, *30*, 2119–2136. [CrossRef]
6. Maltamo, M.; Bollandsås, O.M.; Gobakken, T.; Næsset, E. Large-scale prediction of aboveground biomass in heterogeneous mountain forests by means of airborne laser scanning. *Can. J. For. Res.* **2016**, *46*, 1138–1144. [CrossRef]
7. Wang, Y.; Ni, W.; Sun, G.; Chi, H.; Zhang, Z.; Guo, Z. Slope-adaptive waveform metrics of large footprint lidar for estimation of forest aboveground biomass. *Remote Sens. Environ.* **2019**, *224*, 386–400. [CrossRef]
8. Ene, L.T.; Naesset, E.; Gobakken, T.; Gregoire, T.G.; Stahl, G.; Holm, S. A simulation approach for accuracy assessment of two-phase post-stratified estimation in large-area LiDAR biomass surveys. *Remote Sens. Environ.* **2013**, *133*, 210–224. [CrossRef]
9. Zhang, R.; Zhou, X.; Ouyang, Z.; Avitabile, V.; Qi, J.; Chen, J.; Giannico, V. Estimating aboveground biomass in subtropical forests of China by integrating multisource remote sensing and ground data. *Remote Sens. Environ.* **2019**, *232*, 111341. [CrossRef]
10. Searle, E.B.; Chen, H.Y.H. Tree size thresholds produce biased estimates of forest biomass dynamics. *For. Ecol. Manag.* **2017**, *400*, 468–474. [CrossRef]
11. Adnan, S.; Maltamo, M.; Mehtätalo, L.; Ammaturo, R.N.L.; Packalen, P.; Valbuena, R. Determining maximum entropy in 3D remote sensing height distributions and using it to improve aboveground biomass modelling via stratification. *Remote Sens. Environ.* **2021**, *260*, 112464. [CrossRef]
12. Babcock, C.; Finley, A.O.; Andersen, H.E.; Pattison, R.; Cook, B.D.; Morton, D.C.; Alonzo, M.; Nelson, R.; Gregoir, T.; Ene, L.; et al. Geostatistical estimation of forest biomass in interior Alaska combining Landsat-derived tree cover, sampled airborne lidar and field observations. *Remote Sens. Environ.* **2018**, *212*, 212–230. [CrossRef]
13. Liu, Y.; Gong, W.; Xing, Y.; Hu, X.; Gong, J. Estimation of the forest stand mean height and aboveground biomass in Northeast China using SAR Sentinel-1B, multispectral Sentinel-2A, and DEM imagery. *ISPRS J. Photogram. Remote Sens.* **2019**, *151*, 277–289. [CrossRef]
14. Dube, T.; Mutanga, O. Evaluating the utility of the medium-spatial resolution Landsat 8 multispectral sensor in quantifying aboveground biomass in uMgeni catchment, South Africa. *ISPRS J. Photogram. Remote Sens.* **2015**, *101*, 36–46. [CrossRef]
15. Lu, D.; Chen, Q.; Wang, G.; Liu, L.; Li, G.; Moran, E. A survey of remote sensing-based aboveground biomass estimation methods in forest ecosystems. *Int. J. Digit. Earth* **2016**, *9*, 63–105. [CrossRef]

16. Karila, K.; Yu, X.; Vastaranta, M.; Karjalainen, M.; Puttonen, E.; Hyyppä, J. TanDEM-X digital surface models in boreal forest above-ground biomass change detection. *ISPRS J. Photogram. Remote Sens.* **2019**, *148*, 174–183. [CrossRef]
17. Cartus, O.; Santoro, M.; Kellndorfer, J. Mapping forest aboveground biomass in the Northeastern United States with ALOS PALSAR dual-polarization L-band. *Remote Sens. Environ.* **2012**, *124*, 466–478. [CrossRef]
18. Poorazimy, M.; Shataee, S.; McRoberts, R.E.; Mohammadi, J. Integrating airborne laser scanning data, space-borne radar data and digital aerial imagery to estimate aboveground carbon stock in Hyrcanian forests, Iran. *Remote Sens. Environ.* **2020**, *240*, 111669. [CrossRef]
19. Ma, J.; Xiao, X.; Qin, Y.; Chen, B.; Hu, Y.; Li, X.; Zhao, B. Estimating aboveground biomass of broadleaf, needleleaf, and mixed forests in Northeastern China through analysis of 25-m ALOS/PALSAR mosaic data. *For. Ecol. Manag.* **2017**, *389*, 199–210. [CrossRef]
20. Ningthoujam, R.K.; Joshi, P.K.; Roy, P.S. Retrieval of forest biomass for tropical deciduous mixed forest using ALOS PALSAR mosaic imagery and field plot data. *Int. J. Appl. Earth Obs. Geoinf.* **2018**, *69*, 206–216. [CrossRef]
21. Carreiras, J.M.B.; Vasconcelos, M.J.; Lucas, R.M. Understanding the relationship between aboveground biomass and ALOS PALSAR data in the forests of Guinea-Bissau (West Africa). *Remote Sens. Environ.* **2012**, *121*, 426–442. [CrossRef]
22. Baig, S.; Qazi, W.A.; Akhtar, A.M.; Waqar, M.M.; Ammar, A.; Gilani, H.; Mehmood, S.A. Above ground biomass estimation of *Dalbergia sissoo* forest plantation from dual-polarized ALOS-2 PALSAR data. *Can. J. Remote Sens.* **2017**, *43*, 297–308. [CrossRef]
23. Castillo, J.A.A.; Apan, A.A.; Maraseni, T.N.; Salmo III, S.G. Estimation and mapping of above-ground biomass of mangrove forests and their replacement land uses in the Philippines using Sentinel imagery. *ISPRS J. Photogram. Remote Sens.* **2017**, *134*, 70–85. [CrossRef]
24. Forkuor, G.; Zoungrana, J.B.B.; Dimobe, K.; Ouattara, B.; Vadrevu, K.P.; Tondoh, J.E. Above-ground biomass mapping in West African dryland forest using Sentinel-1 and 2 datasets—A case study. *Remote Sens. Environ.* **2020**, *236*, 111496. [CrossRef]
25. Aslan, A.; Rahman, A.F.; Robeson, S.M. Investigating the use of Alos Prism data in detecting mangrove succession through canopy height estimation. *Ecol. Indic.* **2018**, *87*, 136–143. [CrossRef]
26. Florinsky, I.V.; Skrypitsyna, T.N.; Luschikova, O.S. Comparative accuracy of the AW3D30 DSM, ASTER GDEM, and SRTM1 DEM: A case study on the Zaoksky testing ground, Central European Russia. *Remote Sens. Lett.* **2018**, *9*, 706–714. [CrossRef]
27. Narine, L.L.; Popescu, S.; Neuenschwander, A.; Zhou, T.; Srinivasan, S.; Harbeck, K. Estimating aboveground biomass and forest canopy cover with simulated ICESat-2 data. *Remote Sens. Environ.* **2019**, *224*, 1–11. [CrossRef]
28. Hernández-Stefanoni, J.L.; Castillo-Santiago, M.Á.; Mas, J.F.; Wheeler, C.E.; Andres-Mauricio, J.; Tun-Dzul, F.; George-Chacón, S.P.; Reyes-Palomeque, G.; Castellanos-Basto, B.; Vaca, R.; et al. Improving aboveground biomass maps of tropical dry forests by integrating LiDAR, ALOS PALSAR, climate and field data. *Carbon Balance Manag.* **2020**, *15*, 15. [CrossRef]
29. Narine, L.L.; Popescu, S.; Zhou, T.; Srinivasan, S.; Harbeck, K. Mapping forest aboveground biomass with a simulated ICESat-2 vegetation canopy product and Landsat data. *Ann. For. Res.* **2019**, *62*, 69–86. [CrossRef]
30. Dubayah, R.; Blair, J.B.; Goetz, S.; Fatoyinbo, L.; Hansen, M.; Healey, S.; Hofton, M.; Hurtt, G.; Kellner, J.; Luthcke, S.; et al. The Global Ecosystem Dynamics Investigation: High-resolution laser ranging of the Earth's forests and topography. *Sci. Remote Sens.* **2020**, *1*, 100002. [CrossRef]
31. Li, W.; Niu, Z.; Shang, R.; Qin, Y.; Wang, L.; Chen, H. High-resolution mapping of forest canopy height using machine learning by coupling ICESat-2 LiDAR with Sentinel-1, Sentinel-2 and Landsat-8 data. *Int. J. Appl. Earth Obs. Geoinf.* **2020**, *92*, 102163. [CrossRef]
32. Potapov, P.; Li, X.; Hernandez-Serna, A.; Tyukavina, A.; Hansen, M.C.; Kommareddy, A.; Pickens, A.; Turubanova, S.; Tang, H.; Silva, C.E.; et al. Mapping global forest canopy height through integration of GEDI and Landsat data. *Remote Sens. Environ.* **2021**, *253*, 112165. [CrossRef]
33. Duncanson, L.; Neuenschwander, A.; Hancock, S.; Thomas, N.; Fatoyinbo, T.; Simard, M.; Silva, C.A.; Armston, J.; Luthcke, S.B.; Hofton, M.; et al. Biomass estimation from simulated GEDI, ICESat-2 and NISAR across environmental gradients in Sonoma County, California. *Remote Sens. Environ.* **2020**, *242*, 111779. [CrossRef]
34. Shen, W.; Li, M.; Huang, C.; Tao, X.; Wei, A. Annual forest aboveground biomass changes mapped using ICESat/GLAS measurements, historical inventory data, and time-series optical and radar imagery for Guangdong province, China. *Agric. For. Meteorol.* **2018**, *259*, 23–38. [CrossRef]
35. Fayad, I.; Baghdadi, N.; Guitet, S.; Bailly, J.S.; Hérault, B.; Gond, V.; El Hajj, M.; Minh, D.H.T. Aboveground biomass mapping in French Guiana by combining remote sensing, forest inventories and environmental data. *Int. J. Appl. Earth Obs. Geoinf.* **2016**, *52*, 502–514. [CrossRef]
36. Urbazaev, M.; Thiel, C.; Cremer, F.; Dubayah, R.; Migliavacca, M.; Reichstein, M.; Schmullius, C. Estimation of forest aboveground biomass and uncertainties by integration of field measurements, airborne LiDAR, and SAR and optical satellite data in Mexico. *Carbon Balance Manag.* **2018**, *13*, 5. [CrossRef]
37. Wang, Y.; Zhang, X.; Guo, Z. Estimation of tree height and aboveground biomass of coniferous forests in North China using stereo ZY-3, multispectral Sentinel-2, and DEM data. *Ecol. Indic.* **2021**, *126*, 107645. [CrossRef]
38. Huang, H.; Liu, C.; Wang, X.; Zhou, X.; Gong, P. Integration of multi-resource remotely sensed data and allometric models for forest aboveground biomass estimation in China. *Remote Sens. Environ.* **2019**, *221*, 225–234. [CrossRef]

39. Wang, D.; Wan, B.; Liu, J.; Su, Y.; Guo, Q.; Qiu, P.; Wu, X. Estimating aboveground biomass of the mangrove forests on northeast Hainan Island in China using an upscaling method from field plots, UAV-LiDAR data and Sentinel-2 imagery. *Int. J. Appl. Earth Obs. Geoinf.* **2020**, *85*, 101986. [CrossRef]

40. Silveira, E.M.O.; Silva, S.H.G.; Acerbi-Junior, F.W.; Carvalho, M.C.; Carvalho, L.M.T.; Scolforo, J.R.S.; Wulder, M.A. Object-based random forest modelling of aboveground forest biomass outperforms a pixel-based approach in a heterogeneous and mountain tropical environment. *Int. J. Appl. Earth Obs. Geoinf.* **2019**, *78*, 175–188. [CrossRef]

41. Wang, Y.; Wu, Z.; Yuan, X.; Zhang, H.; Zhang, J.; Xu, J.; Lu, Z.; Zhou, Y.; Feng, J. Resources and ecological security of the Changbai Mountain region in Northeast Asia. In *Remote Sensing of Protected Lands*; Wang, Y.Q., Ed.; CRC Press: Boca Raton, FL, USA, 2011.

42. Dai, L.; Jia, J.; Yu, D.; Lewis, B.J.; Zhou, L.; Zhou, W.; Zhao, W.; Jiang, L. Effects of climate change on biomass carbon sequestration in old-growth forest ecosystems on Changbai Mountain in Northeast China. *For. Ecol. Manag.* **2013**, *300*, 106–116. [CrossRef]

43. Chen, L.; Ren, C.; Zhang, B.; Wang, Z.; Wang, Y. Mapping spatial variations of structure and function parameters for forest condition assessment of the Changbai Mountain National Nature Reserve. *Remote Sens.* **2019**, *11*, 3004. [CrossRef]

44. Yang, X.; Xu, M. Biodiversity conservation in Changbai Mountain Biosphere Reserve, northeastern China: Status, problem, and strategy. *Biodivers. Conserv.* **2003**, *12*, 883–903. [CrossRef]

45. Xu, Z.; Yu, G.; Zhang, X.; Ge, J.; He, N.; Wang, Q.; Wang, D. The variations in soil microbial communities, enzyme activities and their relationships with soil organic matter decomposition along the northern slope of Changbai Mountain. *Appl. Soil Ecol.* **2015**, *86*, 19–29. [CrossRef]

46. Zhou, G.; Yi, G.; Tang, X.; Wen, Z.; Liu, C.; Kuang, Y.; Wang, W. *Carbon Stock of Forest Ecosystems in China—Biomass Equations*; Science Press: Beijing, China, 2018.

47. Popescu, S.C.; Zhao, K.; Neuenschwander, A.; Lin, C. Satellite lidar vs. small footprint airborne lidar: Comparing the accuracy of aboveground biomass estimates and forest structure metrics at footprint level. *Remote Sens. Environ.* **2011**, *115*, 2786–2797. [CrossRef]

48. Zald, H.S.J.; Wulder, M.A.; White, J.C.; Hilker, T.; Hermosilla, T.; Hobart, G.W.; Coops, N.C. Integrating Landsat pixel composites and change metrics with lidar plots to predictively map forest structure and aboveground biomass in Saskatchewan, Canada. *Remote Sens. Environ.* **2016**, *176*, 188–201. [CrossRef]

49. Ni-Meister, W.; Jupp, D.L.B.; Dubayah, R. Modeling lidar waveforms in heterogeneous and discrete canopies. *IEEE Trans. Geosci. Remote Sens.* **2001**, *39*, 1943–1958. [CrossRef]

50. Silva, C.A.; Hamamura, C.; Valbuena, R.; Hancock, S.; Cardil, A.; Broadbent, E.N.; Almeida, D.R.A.; Silva Junior, C.H.L.; Klauberg, C. rGEDI: NASA's Global Ecosystem Dynamics Investigation (GEDI) Data Visualization and Processing, version 0.1.2. 2020. Available online: https://CRAN.R-project.org/package=rGEDI (accessed on 1 April 2020).

51. Neuenschwander, A.; Pitts, K. The ATL08 land and vegetation product for the ICESat-2 Mission. *Remote Sens. Environ.* **2019**, *221*, 247–259. [CrossRef]

52. NSIDC. ATL08 Product Data Dictionary. 2020. Available online: https://nsidc.org/sites/nsidc.org/files/technical-references/ICESat2_ATL08_data_dict_v003.pdf (accessed on 3 February 2020).

53. Hird, J.N.; DeLancey, E.R.; McDermid, G.J.; Kariyeva, J. Google Earth Engine, open-access satellite data, and machine learning in support of large-area probabilistic wetland mapping. *Remote Sens.* **2017**, *9*, 1315. [CrossRef]

54. Chen, L.; Ren, C.; Zhang, B.; Wang, Z.; Liu, M.; Man, W.; Liu, J. Improved estimation of forest stand volume by the integration of GEDI LiDAR data and multi-sensor imagery in the Changbai Mountains Mixed Forests Ecoregion (CMMFE), Northeast China. *Int. J. Appl. Earth Obs. Geoinf.* **2021**, *100*, 102326. [CrossRef]

55. Aslan, A.; Rahman, A.F.; Warren, M.W.; Robeson, S.M. Mapping spatial distribution and biomass of coastal wetland vegetation in Indonesian Papua by combining active and passive remotely sensed data. *Remote Sens. Environ.* **2016**, *183*, 65–81. [CrossRef]

56. Chen, L.; Wang, Y.; Ren, C.; Zhang, B.; Wang, Z. Assessment of multi-wavelength SAR and multispectral instrument data for forest aboveground biomass mapping using random forest kriging. *For. Ecol. Manag.* **2019**, *447*, 12–25. [CrossRef]

57. Nie, S.; Wang, C.; Zeng, H.; Xi, X.; Li, G. Above-ground biomass estimation using airborne discrete-return and full-waveform LiDAR data in a coniferous forest. *Ecol. Indic.* **2017**, *78*, 221–228. [CrossRef]

58. Bell, D.M.; Gregory, M.J.; Kane, V.; Kane, J.; Kennedy, R.E.; Roberts, H.M.; Yang, Z. Multiscale divergence between Landsat- and lidar-based biomass mapping is related to regional variation in canopy cover and composition. *Carbon Balance Manag.* **2018**, *13*, 15. [CrossRef]

59. Brunsdon, C.; Fotheringham, A.S.; Charlton, M.E. Geographically weighted regression: A method for exploring spatial nonstationarity. *Geogr. Anal.* **1996**, *28*, 281–298. [CrossRef]

60. Brunsdon, C.; Fotheringham, A.S.; Charlton, M.E. Geographically Weighted Regression–Modelling Spatial Non-stationarity. In *Workshop on Local Indicators of Spatial Association*; University of Leicester: Leicester, UK, 1998.

61. Chen, L.; Ren, C.; Zhang, B.; Wang, Z.; Xi, Y. Estimation of forest above-ground biomass by geographically weighted regression and machine learning with Sentinel imagery. *Forests* **2018**, *9*, 582. [CrossRef]

62. Fotheringham, A.S.; Brunsdon, C.; Charlton, M.E. *Geographically Weighted Regression: The Analysis of Spatially Varying Relationships*; Wiley: Chichester, UK, 2002.

63. Nakaya, T.; Charlton, M.; Lewis, P.; Brunsdon, C.; Yao, J.; Fotheringham, S. *GWR4 User Manual, Windows Application for Geographically Weighted Regression Modelling*; Ritsumeikan University: Kyoto, Japan, 2014.

64. Ahmed, M.A.A.; Abd-Elrahman, A.; Escobedo, F.J.; Cropper, W.P.; Martin, T.A.; Timilsina, N. Spatially-explicit modeling of multi-scale drivers of aboveground forest biomass and water yield in watersheds of the Southeastern United States. *J. Environ. Manag.* **2017**, *199*, 158–171. [CrossRef] [PubMed]

65. Jia, M.; Mao, D.; Wang, Z.; Ren, C.; Zhu, Q.; Li, X.; Zhang, Y. Tracking long-term floodplain wetland changes: A case study in the China side of the Amur River Basin. *Int. J. Appl. Earth Obs. Geoinf.* **2020**, *92*, 102185. [CrossRef]

66. Drăguţ, L.; Tiede, D.; Levick, S.R. ESP: A tool to estimate scale parameter for multiresolution image segmentation of remotely sensed data. *Int. J. Geogr. Inf. Sci.* **2010**, *24*, 859–871. [CrossRef]

67. Fassnacht, F.E.; Poblete-Olivares, J.; Rivero, L.; Lopatin, J.; Ceballos-Comisso, A.; Galleguillos, M. Using Sentinel-2 and canopy height models to derive a landscape-level biomass map covering multiple vegetation types. *Int. J. Appl. Earth Obs. Geoinf.* **2021**, *94*, 102236. [CrossRef]

68. Genuer, R.; Poggi, J.-M.; Tuleau-Malot, C. VSURF: An R package for variable selection using random forests. *R J. R Found. Stat. Comput.* **2015**, *7*, 19–33. [CrossRef]

69. Puliti, S.; Hauglin, M.; Breidenbach, J.; Montesano, P.; Neigh, C.S.R.; Rahlf, J.; Solberg, S.; Klingenberg, T.F.; Astrup, R. Modelling above-ground biomass stock over Norway using national forest inventory data with ArcticDEM and Sentinel-2 data. *Remote Sens. Environ.* **2020**, *236*, 111501. [CrossRef]

70. Wittke, S.; Yu, X.W.; Karjalainen, M.; Hyyppä, J.; Puttonen, E. Comparison of two-dimensional multitemporal Sentinel-2 data with three dimensional remote sensing data sources for forest inventory parameter estimation over a boreal forest. *Int. J. Appl. Earth Obs. Geoinf.* **2019**, *76*, 167–178. [CrossRef]

71. Laurin, G.V.; Pirotti, F.; Callegari, M.; Chen, Q.; Cuozzo, G.; Lingua, E.; Notarnicola, C.; Papale, D. Potential of ALOS2 and NDVI to estimate forest above-ground biomass, and comparison with Lidar-derived estimates. *Remote Sens.* **2017**, *9*, 18. [CrossRef]

72. Sinha, S.; Santra, A.; Sharma, L.; Jeganathan, C.; Nathawat, M.S.; Das, A.K.; Mohan, S. Multi-polarized Radarsat-2 satellite sensor in assessing forest vigor from above ground biomass. *J. For. Res.* **2018**, *29*, 1139–1145. [CrossRef]

73. Astola, H.; Häme, T.; Sirro, L.; Molinier, M.; Kilpi, J. Comparison of Sentinel-2 and Landsat 8 imagery for forest variable prediction in boreal region. *Remote Sens. Environ.* **2019**, *223*, 257–273. [CrossRef]

74. Rodríguez-Veiga, P.; Quegan, S.; Carreiras, J.; Persson, H.J.; Fransson, J.E.S.; Hoscilo, A.; Ziółkowski, D.; Stereńczak, K.; Lohberger, S.; Stängel, M.; et al. Forest biomass retrieval approaches from earth observation in different biomes. *Int. J. Appl. Earth Obs. Geoinf.* **2019**, *77*, 53–68. [CrossRef]

75. Silva, C.A.; Duncanson, L.; Hancock, S.; Neuenschwander, A.; Thomas, N.; Hofton, M.; Fatoyinbo, L.; Simard, M.; Marshak, C.Z.; Armston, J.; et al. Fusing simulated GEDI, ICESat-2 and NISAR data for regional aboveground biomass mapping. *Remote Sens. Environ.* **2021**, *253*, 112234. [CrossRef]

76. Chi, H.; Sun, G.; Huang, J.; Li, R.; Ren, X.; Ni, W.; Fu, A. Estimation of forest aboveground biomass in Changbai Mountain region using ICESat/GLAS and Landsat/TM data. *Remote Sens.* **2017**, *9*, 707. [CrossRef]

77. Shen, C.; Liang, W.; Shi, Y.; Lin, X.; Zhang, H.; Wu, X.; Xie, G.; Chain, P.; Grogan, P.; Chu, H. Contrasting elevational diversity patterns between eukaryotic soil microbes and plants. *Ecology* **2014**, *95*, 3190–3202. [CrossRef]

78. Cong, Y.; Li, M.; Liu, K.; Dang, Y.; Han, H.; He, H. Decreased temperature with increasing elevation decreases the end-season leaf-to-wood reallocation of resources in deciduous Betula ermanii Cham. Trees. *Forests* **2019**, *10*, 166. [CrossRef]

79. Yuan, Z.; Ali, A.; Jucker, T.; Ruiz-Benito, P.; Wang, S.; Jiang, L.; Wang, X.; Lin, F.; Ye, J.; Hao, Z.; et al. Multiple abiotic and biotic pathways shape biomass demographic processes in temperate forests. *Ecology* **2019**, *100*, e02650. [CrossRef] [PubMed]

80. Puliti, S.; Saarela, S.; Gobakken, T.; Ståhl, G.; Naesset, E. Combining UAV and Sentinel-2 auxiliary data for forest growing stock volume estimation through hierarchical model-based inference. *Remote Sens. Environ.* **2018**, *204*, 485–497. [CrossRef]

81. Sinha, S.; Jeganathan, C.; Sharma, L.K.; Nathawat, M.S. A review of radar remote sensing for biomass estimation. *Int. J. Environ. Sci. Technol.* **2015**, *12*, 1779–1792. [CrossRef]

82. Morin, D.; Planells, M.; Guyon, D.; Villard, L.; Mermoz, S.; Bouvet, A.; Thevenon, H.; Dejoux, J.-F.; Toan, T.L.; Dedieu, G. Estimation and mapping of forest structure parameters from open access satellite images: Development of a generic method with a study case on coniferous plantation. *Remote Sens.* **2019**, *11*, 1275. [CrossRef]

83. Lefsky, M.A.; Cohen, W.B.; Acker, S.A.; Parker, G.G.; Spies, T.A.; Harding, D. Lidar remote sensing of the canopy structure and biophysical properties of Douglas-Fir Western Hemlock Forests. *Remote Sens. Environ.* **1999**, *70*, 339–361. [CrossRef]

84. Rodríguez-Veiga, P.; Saatchi, S.; Tansey, K.; Balzter, H. Magnitude, spatial distribution and uncertainty of forest biomass stocks in Mexico. *Remote Sens. Environ.* **2016**, *183*, 265–281. [CrossRef]